Aeroelastic Tailoring of Transport Wings Including Transonic Flutter Constraints

Bret K. Stanford[1], Carol D. Wieseman[2]
NASA Langley Research Center, Hampton, VA, 23681

Christine V. Jutte[3]
Craig Technologies, Inc., Cape Canaveral, FL, 32920

Several minimum-mass optimization problems are solved to evaluate the effectiveness of a variety of novel tailoring schemes for subsonic transport wings. Aeroelastic stress and panel buckling constraints are imposed across several trimmed static maneuver loads, in addition to a transonic flutter margin constraint, captured with aerodynamic influence coefficient-based tools. Tailoring with metallic thickness variations, functionally graded materials, balanced or unbalanced composite laminates, curvilinear tow steering, and distributed trailing edge control effectors are all found to provide reductions in structural wing mass with varying degrees of success. The question as to whether this wing mass reduction will offset the increased manufacturing cost is left unresolved for each case.

I. Introduction

Recent work [1] by the authors has considered the static aeroelastic tailoring of a subsonic transport wing box, as part of NASA's Subsonic Fixed Wing project (within the Fundamental Aeronautics program). The optimization studies in that paper sought to minimize the structural wing mass, subject to stress and panel buckling constraints spread over a set of load cases. A variety of aeroelastic tailoring technologies were considered, including localized shell thickness variations, functionally graded metals (FGM) [2][3], composite skin laminates, curvilinear tow steered composites [4][5], and a continuous trailing edge flap [6]. The latter category involves simultaneously optimizing the wing structural details and the scheduling of distributed control surfaces across multiple load cases. Though optimizing the scheduling of a continuous trailing edge flap may seem to be a large conceptual departure from the other structural-design methods, distributed control surfaces may be equally adept at tailoring load paths throughout a wing structure. Furthermore, from an aeroelastic sensitivity and optimization perspective, control surface deflection terms and explicit structural sizing/stiffness terms are handled in very similar ways, as will be seen.

The authors' past work in Ref. [1] has taken a relatively small subset of the load cases and design metrics that are typically considered during wing design in industry [7], in an effort to distill the situation down to its fundamental aspects, and make comparative rankings of various aeroelastic tailoring strategies. However, one obvious omission is a dynamic flutter constraint: an explosive and catastrophic failure mode that can play a key role in the design process. The results presented in this paper augment the results of Ref. [1] with a transonic flutter constraint, and also provide further additions/modifications to the structural parameterizations utilized previously.

The doublet lattice method (DLM) is, historically, the industry-accepted tool for flutter prediction of aircraft [8]. The appeal of the method, particularly from an aeroelastic optimization perspective, lies in the aerodynamic influence coefficients (AICs). AICs are complex matrices that govern the relationship between pressure and downwash at a set number of reduced frequencies. As they are independent of the structural details of the wing, they can be computed once, and used repetitively during the optimization process. The transport configurations studied here fly in the transonic range; however, the mixed characteristics of the flow over the wing (subsonic base flow with a supersonic bubble on the upper wing surface) increase the nonlinearities within the flutter mechanism.

---

[1] Research Aerospace Engineer, Aeroelasticity Branch, bret.k.stanford@nasa.gov, AIAA Member.
[2] Research Aerospace Engineer, Aeroelasticity Branch, carol.d.wieseman@nasa.gov, AIAA Member.
[3] Research Engineer, Advanced Materials and Processing Branch, christine.v.jutte@nasa.gov, AIAA Member.

The accuracy of the linear DLM is typically compromised in the transonic regime, unless augmented with wind tunnel data [8], which does not exist for the conceptual configuration studied here.

Alternatively, computational fluid dynamics may be expected to accurately predict the nonlinear flutter mechanisms. CFD-based flutter analysis can be conducted in the time domain, the frequency domain [9], or using a direct Hopf-bifurcation method [10]. Any unsteady CFD-based method is very expensive, however, and ill-suited for the repetitive nature of design optimization. A compromise is utilized here, in the form of the ZTRAN flutter tool [11]. This method uses fully nonlinear CFD (the Euler code ZEUS is used for the present work) to compute the steady transonic flow over the transport wing. Linearization about the steady background flow is then carried out for a range of reduced frequencies (via the time-linearized transonic small disturbance equations) and interpolated onto a flat-plate wing mesh with a field panel scheme. This is highly conducive to aeroelastic optimization, in that these transonic AICs, like their linear DLM counterparts, can be computed a single time off-line, and then used for the duration of the optimization process. These transonic AICs are in fact dependent upon the wing shape and angle of attack used to compute the steady background flow, a dependency that increases with Mach number [9]. During aeroelastic optimization, the trimmed 1-g flying wing shape will change somewhat as material is removed or added to the wing, but this effect is ignored here, and constant values are used for the purposes of the flutter analysis. Trim wing shapes are properly updated for the static aeroelastic load cases, however.

This work is organized as follows. A description of the subsonic transport aircraft and the aeroelastic tools used here are provided first. Then a minimum-mass aeroelastic optimization problem is formulated and solved using simple patch thickness design variables. The various members of the wing box (skins, spars, ribs, stringers) are divided into large design segments (patches), and the optimal thickness of each patch is found. This type of structural wing design is within the state-of-the-art, and so the resulting design is termed the "baseline", whose mass is repeatedly compared to the minimum mass obtained with more sophisticated aeroelastic tailoring methods. These include methods enabled by additive manufacturing, such as finely-detailed thickness distributions and/or FGM. Composite laminates are considered with straight fibers within each design segment as well as tow steered fibers. Balanced and unbalanced laminates are both utilized, where the former stipulates that the number of plies in the θ direction must equal the number in the $-\theta$ direction. Finally, the scheduling of distributed trailing edge control surfaces are optimized as well.

II. The Common Research Model

All of the work in this paper is conducted on the conceptual Common Research Model (CRM) seen in Figure 1. This transonic transport configuration has a wing span of 58.7 m, a mean aerodynamic chord of 7.0 m, an aspect ratio of 9, a taper ratio of 0.275, a sweep angle of 35°, and a cruise Mach number of 0.85. The outer mold line given in Ref. [12] is a 1-g cruise shape, so a standard inverse method is used here to obtain the jig shape seen in Figure 1. A wing box structure is developed, which consists of an upper skin, a lower skin, a leading edge spar (located at 12% of the local airfoil chord), a trailing edge spar (located at 71% chord), 27 ribs, and 6 run-out stringers (linearly tapered from a depth of 15 cm at the root to 5 cm at the tip). These members are discretized into 92,000 triangular shell finite elements to form a model with 270,000 degrees of freedom.

The structure within the leading and trailing edges of the wing is not explicitly modeled, though an inertial effect is captured with a series of lumped masses attached to the wing box via interpolation elements. These masses, along with similar representations for the engine and the fuel, are also shown in Figure 1. In addition to the inertial loads from the lumped masses, a thrust force is applied to the central engine node. Aerodynamic paneling for the wing, horizontal tail, vertical tail, fuselage, and engine (the latter two represented as cruciforms) is shown in the figure as well, with a total of 4,700 panels. Control surfaces (either along the wing's trailing edge or the tail's elevator) are not explicitly modeled structurally. Instead, surface deflection is modeled by altering the downwash within the appropriate aerodynamic panels, and the change in aerodynamic loading is implicitly transmitted into the wing structure via the spline-based interpolation methods described below.

III. Aeroelastic Modeling and Sensitivities

This aeroelastic analysis and sensitivity framework used here is developed as an in-house MATLAB© code. Analysis results have been extensively verified for accuracy against MSC NASTRAN's aeroelastic solvers.

A. Static Aeroelastic Trim Loads

The shell finite elements used to model the wing structure are defined by a combination of linear strain triangles (LST) and discrete Kirchhoff triangles (DKT) [13]. For static airloads, a linear vortex lattice method [14] is used to model the aerodynamic lifting surfaces. This tool cannot properly account for transonic effects, though the linear

deficiency should be less critical for static trim loading than for the unsteady flutter analysis described below. A finite plate spline (FPS) method [15] is used to transfer downwash and pressures between the aerodynamic and structural modules. Only information pertaining to the wing is transferred in this way: the remaining aerodynamic surfaces are not explicitly tied to any structure.

The wing box structure is sized across two different types of static maneuvers. The first type is a longitudinal maneuver (pull-up, push-over), where the system is trimmed via the angle of attack α and the elevator deflection δ. Following methods outlined in Ref. [16], the trimmed values of these two quantities are automatically found by augmenting the aero-structural coupling equations. The final equation for a longitudinal maneuver is written as:

$$\begin{bmatrix} \boldsymbol{K} & -q\cdot\boldsymbol{Q} & \boldsymbol{0} & \boldsymbol{0} \\ -\boldsymbol{P} & \boldsymbol{D}^{s} & -\boldsymbol{L}_{\alpha} & -\boldsymbol{L}_{\delta} \\ \boldsymbol{0} & q\cdot\boldsymbol{S}_{\boldsymbol{L}}^{T} & 0 & 0 \\ \boldsymbol{0} & q\cdot\boldsymbol{S}_{\boldsymbol{m}}^{T} & 0 & 0 \end{bmatrix} \cdot \begin{Bmatrix} \boldsymbol{u} \\ \boldsymbol{C}_{p} \\ \alpha \\ \delta \end{Bmatrix} = \begin{Bmatrix} N\cdot\boldsymbol{F}^{grav}+\boldsymbol{F}^{thrust} \\ \boldsymbol{z}_{x} \\ N\cdot W \\ 0 \end{Bmatrix} + \begin{Bmatrix} \boldsymbol{0} \\ \boldsymbol{L}_{\gamma}\cdot\boldsymbol{\gamma} \\ 0 \\ 0 \end{Bmatrix} \tag{1}$$

The first row of Eq. 1 is the finite element analysis: $\boldsymbol{K}$ is the stiffness matrix, and the solution vector $\boldsymbol{u}$ has six degrees of freedom per node (three displacements and three rotations). Forcing functions include self-weight inertial loading $\boldsymbol{F}^{grav}$ (scaled by the maneuver load factor N, and accounting for both the weight of the wing structure and the lumped masses in Figure 1), thrust loading $\boldsymbol{F}^{thrust}$ from the engine, and aerodynamic forces. Aerodynamic forces are written as $q\cdot\boldsymbol{Q}\cdot\boldsymbol{C}_p$, where $\boldsymbol{C}_p$ is a vector of differential pressure coefficients acting on each panel of the vehicle, $\boldsymbol{Q}$ is an interpolation function derived from FPS, and q is the dynamic pressure.

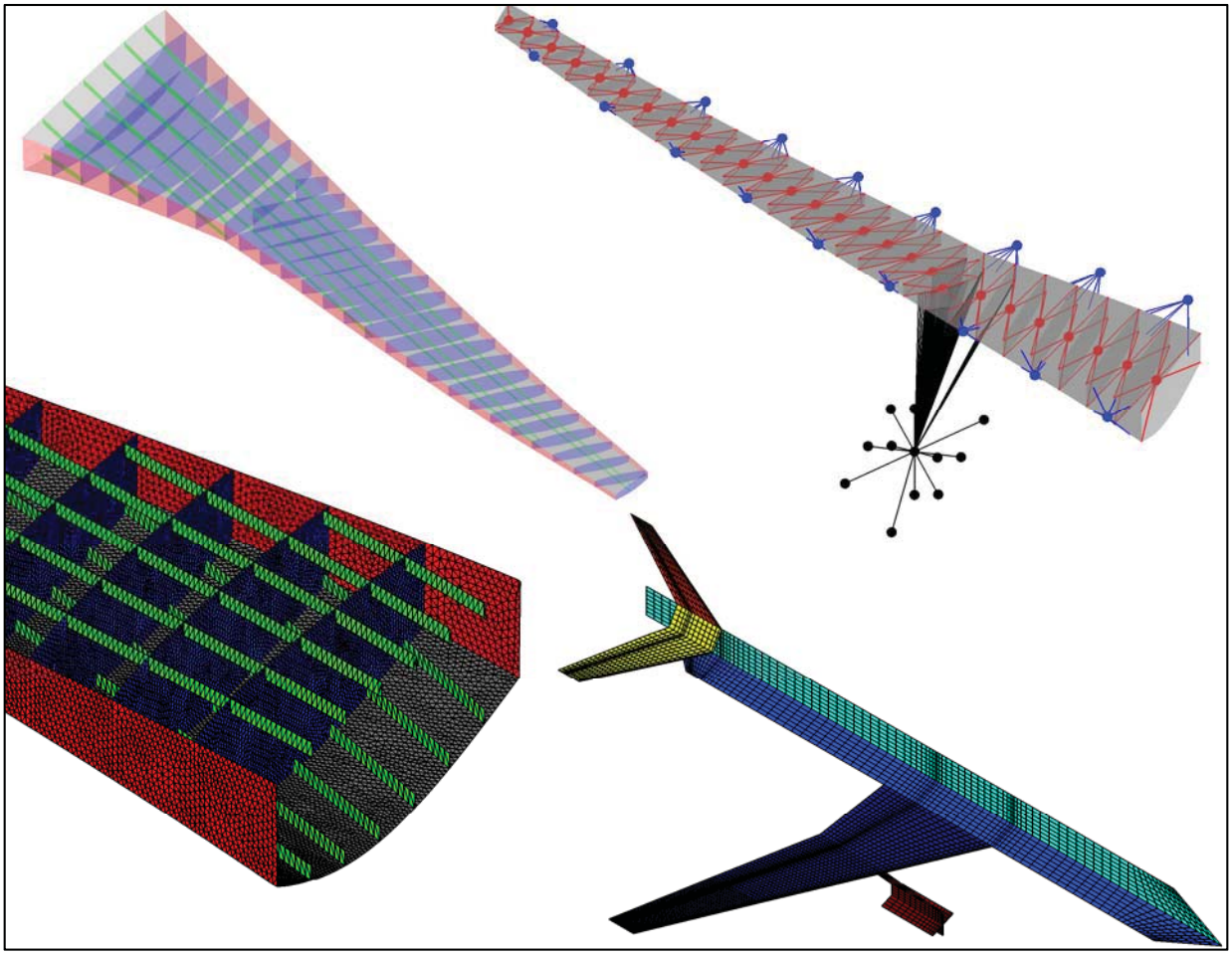

Figure 1. Common Research Model: rib/spar/stringer topology (upper left), lumped-mass representation (upper right), shell-based finite elements (lower left), aerodynamic paneling (lower right).

The second row of Eq. 1 is the aerodynamic analysis, where $\boldsymbol{D}^s$ is the matrix of aerodynamic influence coefficients (AIC) and the superscript indicates a symmetric aerodynamic condition about the centerline of the airplane in Figure 1. This equation is driven by several terms: downwash due to angle of attack $\boldsymbol{L}_\alpha \cdot \alpha$ (where $\boldsymbol{L}_\alpha$ is a linear operator that converts the scalar angle of attack into a downwash at each panel), elevator deflection $\boldsymbol{L}_\delta \cdot \delta$, built in camber/twist of the wing and tail jig shapes $\boldsymbol{z}_x$, and downwash induced by structural wing deformation. This latter term is written as $\boldsymbol{P} \cdot \boldsymbol{u}$, where $\boldsymbol{P}$ is a second interpolation function, also derived from FPS-based methods. A final downwash term is needed if distributed control surfaces are used along the trailing edge during the maneuver. The deflection of each control surface is grouped into the vector $\boldsymbol{\gamma}$, and $\boldsymbol{L}_\gamma$ is a matrix that converts these deflections into the appropriate downwash at each panel.

These deflections $\boldsymbol{\gamma}$ are known, specified quantities during the solution of Eq. 1: α and δ are found that trim the system in the presence of these and other terms. Trim equations are written in the 3rd and 4th rows of Eq. 1: $q \cdot \boldsymbol{S}_L$ and $q \cdot \boldsymbol{S}_m$ convert the differential pressure vector $\boldsymbol{C}_p$ into a total aerodynamic lift and aerodynamic pitching moment (about the aircraft center of gravity). Lift must offset the total weight of the vehicle ($N \cdot W$), and the pitching moment must be zero.

A second type of static maneuver considered here is a rolling trim analysis (Eq. 2), where the deflection β of an outboard wing aileron is found such that a constant specified non-dimensional roll rate $p \cdot L/U$ is maintained, with no rolling acceleration. In this analysis, p is the dimensional roll rate, L is the semi-span, U is the flight speed, and the aileron is placed between 70% and 90% of the semi-span, with a hinge line at 71% of the local chord. The system is simultaneously trimmed longitudinally for steady level flight (N=1) with the angle of attack α. The first analysis requires an anti-symmetric condition about the centerline of the airplane; the second uses a symmetric condition. Owing to the linear nature of the methods used here, structural deformations and aerodynamic pressures for the two conditions can be solved separately, and then added together to obtain the total aeroelastic state [16]. The final equation for this maneuver (rolling at level flight) is written as:

$$\begin{bmatrix} \boldsymbol{K} & \boldsymbol{0} & -q \cdot \boldsymbol{Q} & \boldsymbol{0} & \boldsymbol{0} & \boldsymbol{0} \\ \boldsymbol{0} & \boldsymbol{K} & \boldsymbol{0} & -q \cdot \boldsymbol{Q} & \boldsymbol{0} & \boldsymbol{0} \\ -\boldsymbol{P} & \boldsymbol{0} & \boldsymbol{D}^s & \boldsymbol{0} & -\boldsymbol{L}_\alpha & \boldsymbol{0} \\ \boldsymbol{0} & -\boldsymbol{P} & \boldsymbol{0} & \boldsymbol{D}^a & \boldsymbol{0} & -\boldsymbol{L}_\beta \\ \boldsymbol{0} & \boldsymbol{0} & q \cdot \boldsymbol{S}_L^T & \boldsymbol{0} & 0 & 0 \\ \boldsymbol{0} & \boldsymbol{0} & \boldsymbol{0} & q \cdot \boldsymbol{S}_p^T & 0 & 0 \end{bmatrix} \cdot \begin{Bmatrix} \boldsymbol{u}^s \\ \boldsymbol{u}^a \\ \boldsymbol{C}_p^s \\ \boldsymbol{C}_p^a \\ \alpha \\ \beta \end{Bmatrix} = \begin{Bmatrix} \boldsymbol{F}^{grav} + \boldsymbol{F}^{thrust} \\ \boldsymbol{0} \\ \boldsymbol{z}_x \\ \left(\frac{p \cdot L}{U}\right) \cdot \boldsymbol{L}_p \\ W \\ 0 \end{Bmatrix} + \begin{Bmatrix} \boldsymbol{0} \\ \boldsymbol{0} \\ \boldsymbol{L}_\gamma \cdot \boldsymbol{\gamma}^s \\ \boldsymbol{L}_\gamma \cdot \boldsymbol{\gamma}^a \\ 0 \\ 0 \end{Bmatrix} \tag{2}$$

The s and a superscripts indicate "symmetric" or "anti-symmetric" terms, $q \cdot \boldsymbol{S}_p$ converts the aerodynamic pressures into a rolling moment about the centerline (which is ultimately set to zero for a constant roll rate), and $\boldsymbol{L}_p$ converts the rolling motion into a downwash term. It is also seen that distributed control surfaces along the trailing edge, if used (in addition to the trimmed aileron deflection β), are separated into symmetric and anti-symmetric scheduling.

B. Stresses

Having solved the static trim Eqs. 1 and 2, stresses and strains can be computed for each static load case, and a knock-up (safety) factor of 30% is applied to each elemental stress value. A failure function is then computed for each element: $\boldsymbol{f}(\boldsymbol{u})$, where $\boldsymbol{u} = \boldsymbol{u}^s + \boldsymbol{u}^a$ in the case of Eq. 2. For metallic finite elements, the von Mises failure criteria is used, whereas the Tsai-Wu failure criteria is used for laminated composite elements. The wing structure is then divided into patches (seen in Figure 2, with a total of 527 patches), and the Kreisselmeier-Steinhauser function [17] is used to compress all of the elemental failure function values within a given patch into a single metric. If all of the stress values within a patch are within their failure envelope, the KS function for that patch will be less than one.

C. Panel Buckling

After the stress analysis, a buckling analysis is run for each load case independently. This is done at the panel level, rather than computing buckling factors for the entire wing, in order to reduce the large cost associated with buckling eigenvalue computations, and also as an acknowledgement of the local nature of skin buckling modes. Similar local panel-level analyses (within the context of a wing-level aeroelastic optimization procedure) are also used in Refs. [18] and [19]. These papers use a finite-strip method and a Rayleigh-Ritz method (assumed buckling modes), respectively. The present work employs a full finite element-based buckling analysis within each panel, using sub-structures of the same wing finite element mesh in Figure 1. While more expensive than the previously

mentioned alternatives, this approach allows for more accuracy when a spatial distribution of stiffness and/or mass is desired within each panel.

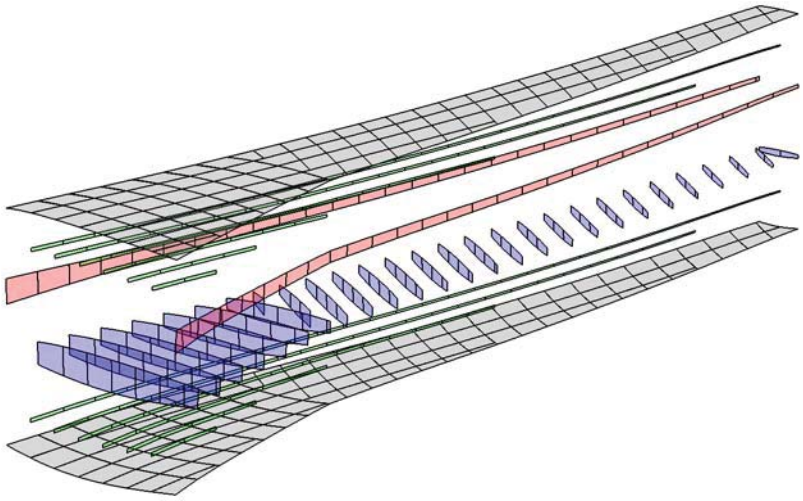

Figure 2. Structural patches used for design variable linking, stress aggregation, and panel identification.

The structural patches in the upper and lower wing skins of Figure 2 are used as panels (210 total), where each panel is bordered along its perimeter by ribs, spars, or stringers. Each finite element buckling sub-problem is solved with a simply-supported boundary condition along this perimeter:

$$\left(\boldsymbol{K}_s(\boldsymbol{u}) + \mu_n \cdot \widetilde{\boldsymbol{K}}\right) \cdot \boldsymbol{v}_n = \boldsymbol{0} \tag{3}$$

where $\boldsymbol{v}_n$ is the eigenvector associated with the n^{th} eigenvalue μ_n. The panel stiffness matrix $\widetilde{\boldsymbol{K}}$ is a subset of the wing matrix $\boldsymbol{K}$ used above, but only including the panel finite elements, and constrained by the simply-supported boundary condition around its perimeter. The panel's geometric stiffness matrix $\boldsymbol{K}_s$ is assembled with element stresses computed from the global wing deformation vector $\boldsymbol{u}$, as solved in Eqs. 1 or 2. An eigenvalue μ_n greater than one indicates that, for the trimmed aeroelastic state computed in Eqs. 1 or 2, the panel has buckled. Two modes are computed for each panel, and a Kreisselmeier-Steinhauser function [17] is again used to compress the eigenvalues in adjacent panels into a smaller number of constraints.

D. Flutter

Flutter analysis is conducted using the same configuration seen in Figure 1, though the aerodynamic paneling of the fuselage, tail, and engine are neglected. A dynamic eigenvalue problem is written as [20]:

$$\left(\frac{U^2}{b^2} \cdot p_n^2 \cdot \bar{\boldsymbol{M}} + \frac{U}{b} \cdot p_n \cdot \bar{\boldsymbol{C}} + \bar{\boldsymbol{K}} - q \cdot \boldsymbol{A}(i \cdot k)\right) \cdot \boldsymbol{u}_n = \boldsymbol{0} \tag{4}$$

where b is half the mean aerodynamic chord, $\boldsymbol{u}_n$ is the eigenvector associated with the n^{th} complex eigenvalue p_n, k is the reduced frequency, $\boldsymbol{M}$ is the mass matrix, $\boldsymbol{C}$ is the damping matrix, and $\boldsymbol{K}$ is the stiffness matrix (identical to that used above). The overbar signifies a reduced term, where the natural vibration mode shapes of the wing have been used to compress full order terms down to modal quantities. The generalized aerodynamic forces $\boldsymbol{A}$ are written in the frequency domain and are computed as follows. For a fixed cruise wing shape, steady background flow is computed with the Euler code ZEUS [9] for a range of Mach numbers. For each flow condition, ZTRAN [11] is used to find AICs for a range of reduced frequencies k. These AICs are converted into $\boldsymbol{A}$ via the FPS-based interpolation functions $\boldsymbol{P}$ and $\boldsymbol{Q}$ from above, as well as the vibration mode shapes.

For a given Mach number, Eq. 4 is solved across a range of matched-point equivalent air speeds using a non-iterative *p-k* method [21]. Speeds at which a given eigenvalue crosses into the right-half plane ($Re(p_n) = 0$) are flutter points. Any flutter point that occurs within the vicinity of the flight envelope by less than a 15% margin (as

measured by equivalent air speed) is considered unacceptable. A variation on the method of Ringertz [22] is used to formulate a flutter constraint. If each eigenvalue is written as $p = g + i \cdot k$, then for a given Mach number, the damping g of each mode is constrained to lie below a given curve at all equivalent air speeds U_{EAS} of interest:

$$g \leq \begin{cases} 0 & 0 \leq U_{EAS} < U^* \\ c \cdot (U_{EAS} - U^*)^2 & U_{EAS} \geq U^* \end{cases} \tag{5}$$

where c is a scaling parameter, and U^* is the minimum allowable flutter equivalent air speed, based on a 15% margin. Critical U_{EAS} points (local minima) of the inequality in Eq. 5 are computed and lumped together into a single Kreisselmeier-Steinhauser constraint. As above, if this constraint is greater than one, then Eq. 5 is not satisfied, and the structure does not meet the required flutter margin. A separate KS constraint is utilized for each considered Mach number.

E. Design Variables and Analytical Sensitivities

Several different types of design variables are used in the exercises described below. Thickness-type variables (either for metallic or composite elements) will have an impact on the wing and panel stiffness matrices $\boldsymbol{K}$, $\widetilde{\boldsymbol{K}}$, and $\boldsymbol{K}_s$, the inertial loading $\boldsymbol{F}^{grav}$, the vehicle weight W, the term $\boldsymbol{S}_m$ (which is dependent upon the center of gravity), the mass matrix $\boldsymbol{M}$, and the damping matrix $\boldsymbol{C}$. Certain material-type variables may impact wing/panel stiffness but not mass, and will only have an effect upon the stiffness matrices. In the event that the scheduling of distributed control effectors are used during the optimization, the relevant design variables are $\boldsymbol{\gamma}^s$ and $\boldsymbol{\gamma}^a$.

Derivatives of the static aeroelastic response (stress and buckling aggregation parameters for each load case) with respect to all design variables are computed with the adjoint method, while sensitivities of the flutter response are computed via nonlinear eigenvalue derivative methods [23]. The nonlinearity here refers not to the transonic effects (the method is entirely linearized with regards to this), but to the fact that $\boldsymbol{A}(i \cdot k)$ is a complex function of the eigenvalue p_n. A free-mode dynamic derivative approach is utilized here, where the derivative of the mode shapes with respect to design variables is neglected for the purposes of gradient computations.

IV. Baseline Model

Considering an all-aluminum wing (E = 70 GPa, ν = 0.3, ρ = 2780 kg/m^3, σ_Y = 330 MPa), the optimal distribution of patch-based thickness variables (using the design patches in Figure 2) are found that minimizes the wing mass (based on the volume of the finite element model) subject to aeroelastic strength, buckling, and flutter constraints:

$$\min_{\boldsymbol{x}} \; mass$$

$$s.t.: \begin{cases} \boldsymbol{0 < x < 1} & \\ KS_{f,i} \leq 1 & i = 1, \dots, (N_f \cdot N_L) \\ KS_{\mu,i} \leq 1 & i = 1, \dots, (N_\mu \cdot N_L) \\ KS_{fl,i} \leq 1 & i = 1, \dots, N_m \end{cases} \tag{6}$$

where $\boldsymbol{x}$ are the thickness design variables that have been appropriately normalized between 0 and 1. Dimensionally, thicknesses are allowed to range between 3 mm and 30 mm. N_L is the number of static load cases, KS_f are the stress aggregation parameters (N_f per load case), KS_μ are the buckling aggregation parameters (N_μ per load case), and KS_{fl} are the flutter aggregation parameters (N_m total Mach numbers considered). Three static load cases are considered for all optimization problems in this paper. Each has a Mach number of 0.85 and a dynamic pressure of 13.8 kPa. The first two load cases are longitudinal maneuvers (Eq. 1), with load factors of 2.5 and -1, respectively. The third load case is dictated by Eq. 2, where the desired non-dimensional roll rate is 0.065. All cases are run with half-fuel, and the distributed control surfaces along the trailing edge (except the aileron deflection β used for lateral trim) are ignored: $\boldsymbol{\gamma = 0}$. A single Mach number of 0.9 is considered for flutter analysis, though as will be seen, the flutter constraint is inactive for this baseline model.

The design variables $\boldsymbol{x}$ are passed through a linearly-decaying cone-shape filter [24] prior to conversion into structural thickness values, in order to prevent the difference in thicknesses between adjacent patches from being too

large. All optimization problems are solved with the Globally-Convergent Method of Moving Asymptotes [25].

The optimal thickness distribution is seen in Figure 3. Only thicknesses in the upper and lower skins are shown, as the optimal rib, spar, and stringer thicknesses are all equal to the lower bound of 3 mm. Upper skins are generally thicker than lower skins, as the pull-up load factor of load case one (2.5g) is greater than the push-over load factor in case two (-1g), and the former will induce buckling in the upper skins. Peak thicknesses occur near the wing break (where the stresses are highest) and taper to the lower bound at the tip, where stresses are very low. These stresses are shown in Figure 4, in the form of von Mises-based failure indices. It should be recalled that this data is not explicitly exposed to the optimizer but is first compressed into KS_f functions. A failure index greater than 1 is indicative of excessive aeroelastic stresses: these constraints are active in several locations throughout the wing. The lower skins are generally higher-stressed than in the upper skin due to the thinner members. Skin and spar stresses for the rolling maneuver case are shifted farther outboard (away from the wing break) than the longitudinal cases, as the former has higher torsional loads than the latter. It is also noted that rib stresses are very low, with the exception of the rib attached to the engine, owing to the localized inertial and thrust loading through that attachment.

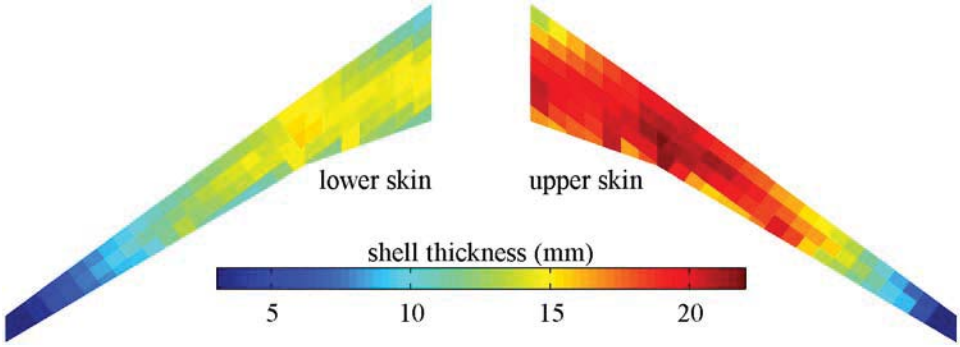

Figure 3. Thickness distribution (mm) of the baseline design: all rib, spar, and stringer thicknesses are at the lower bound (3 mm).

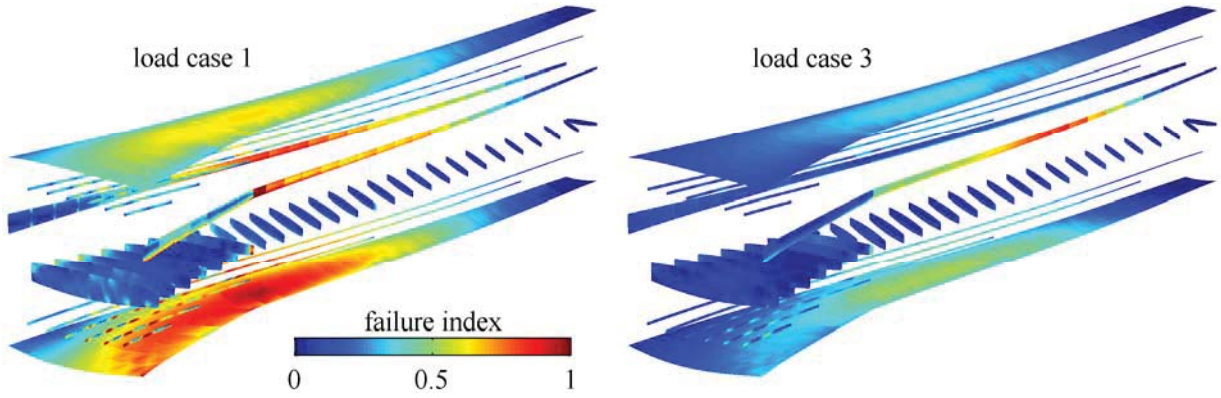

Figure 4. Baseline stress-based failure indices for load case 1 (pull-up maneuver) and 3 (rolling maneuver).

The critical buckling eigenvalues across the panels for each load case are shown in Figure 5. As before, this data is not directly provided to the optimizer but first compressed into a series of KS_μ functions. Panels with a negative eigenvalue are left blank in this figure, as this is a physically meaningless result: for a given maneuver case, the loads would have to be entirely reversed for these panels to buckle. This clearly happens through most of the lower surface during the positive load factors (cases 1 and 3), and through most of the upper surface during the negative load factor (case 2). Otherwise, many of the panels have a buckling factor nearly equal to one (active constraints), and so the conflict between these KS_μ constraints and the wing mass are driving the design process. For the longitudinal maneuvers, the majority of the wing surface has a large buckling factor, even out towards the wing tip where the stresses (used to form $\boldsymbol{K}_s$ in Eq. 3) are very low. Some panels have an active buckling constraint during the rolling maneuver as well, but only in the mid-span location where the stresses in Figure 4 are higher.

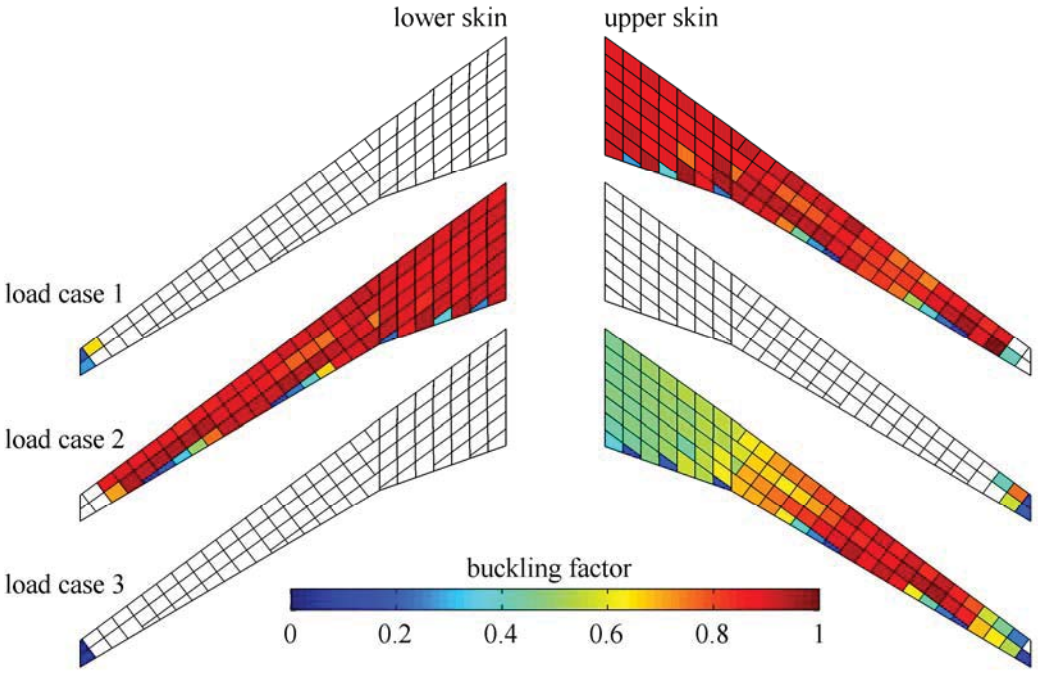

Figure 5. Baseline panel buckling eigenvalues for all three load cases.

The optimal mass of the structure in Figure 3 is 9,081.3 kg; this structure is based on the volume of the finite element model and does not include any of the lumped mass in Figure 1. This mass will be repeatedly compared to the minimum mass obtained with more sophisticated tailoring methods detailed below. The flutter constraint for this baseline structure in Figure 3 is not active: i.e., the flutter margin is greater than the required value of 15%.

A. Buckling-Flutter Pareto Front

As an exercise, the flutter constraint can be made active by relaxing one of the other constraint boundaries. Panel buckling is a good candidate for relaxation, for two reasons. First, the previous figures would indicate that the buckling constraint is more active over a larger fraction of the wing as compared to stresses, and thus a stronger design driver. Secondly, there is a physical rationale for allowing skin buckling in some cases [7], as stiffened panels will continue to carry load beyond the linear buckling point. Using the same design variables as in Figure 3, a series of optimization problems are solved with progressively easier-to-satisfy buckling constraints. The minimum attainable mass can be plotted as a function of the allowable buckling eigenvalue to trace the Pareto front, seen in Figure 6. The mass data point for an allowable buckling factor of one is repeated from above (baseline mass of 9,081.3 kg). Increasing the permissible buckling factors up to six (i.e., each panel is allowed to carry six times the linear buckling load: $KS_\mu \leq 6$) allows for a considerable drop in optimal wing mass: 38.93%.

The flutter margin for the baseline design is 47%, but this flutter constraint becomes active (15% margin) when the allowable buckling factor increases above 2.6, and remains active through the highest buckling factor considered (six). Eigenvalue migration curves (solution to Eq. 4) for this case with the highest buckling factor are shown in Figure 7, where a dashed line is used to indicate the damping constraint boundary of Eq. 5. This constraint is active at the flutter point of mode 2, preserving the required 15% flutter margin. The flutter mechanism seen here is representative of the remaining results in this paper, where the fluttering mode 2 is a torsional hump mode with a substantial degree of engine pitch, which is typical of transport wings [9].

Unless stated otherwise, the remaining results in this paper require KS_μ to be less than one.

V. Additive Manufacturing

Two advances upon the previous baseline exercise are considered here. The first allows for highly localized thickness variations throughout the aluminum wing structure, rather than the patch thickness design variables. The second uses FGM, where the optimizer must make simultaneous choices about the thickness and material distribution through the wing structure. Both techniques require the use of additive manufacturing over large acreage structures, which is not commonly used in current aircraft design.

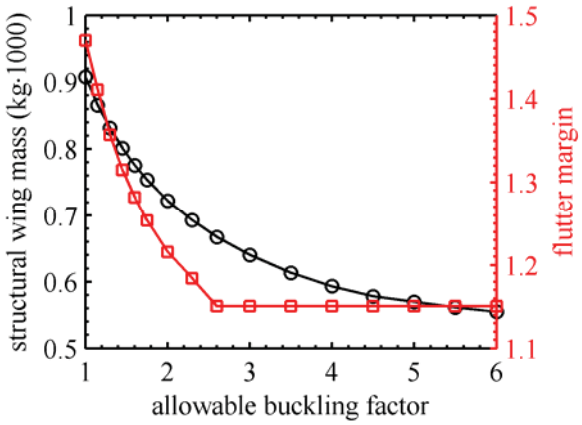

Figure 6. Pareto front between wing mass, flutter margin, and allowable panel buckling factor.

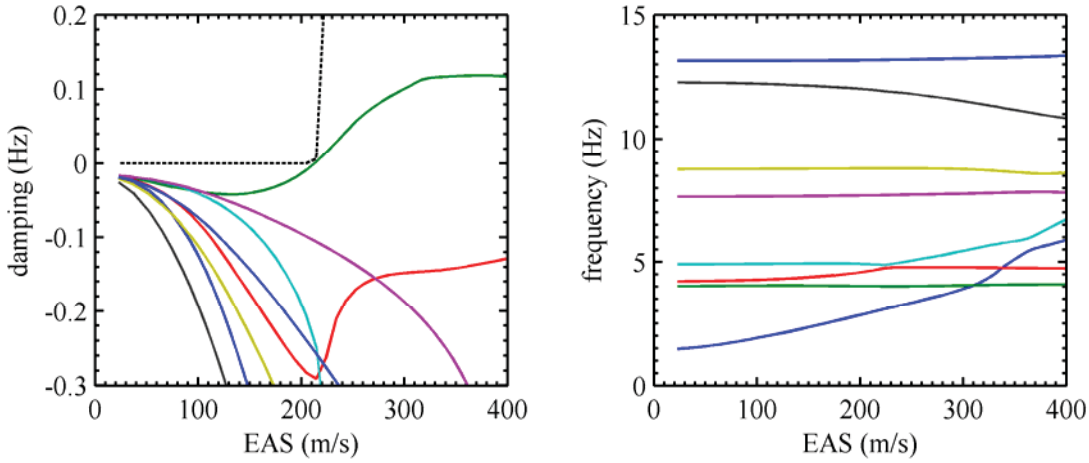

Figure 7. Eigenvalue migration curves for the case in Figure 6 with an allowable buckling factor of six. Dashed line is the damping constraint boundary from Eq. 5.

A. Detailed Thickness Variations

The thickness of every shell finite element is now assigned its own design variable, for 92,000 total design variables, as opposed to 527 for the previous exercise. As noted above, the adjoint method is utilized for the aeroelastic sensitivity analysis, whose computational cost scales weakly with the number of design variables. Cost is proportional to the number of constraints [23], but the KS_f and KS_μ details remain unchanged from the previous case. Design variables are again passed through a linearly-decaying cone-shape filter [24] to ensure a smooth thickness distribution. The radius of this filter is 0.3 m, which is 4.2% of the mean aerodynamic chord.

The optimal thickness distribution for this case is given in Figure 8. Global trends align with that seen for the baseline, with peak thickness at the wing break, minimum thickness at the tip, and thicker panels in the upper skin as compared to the lower. Substantial local variations are evident, however, and are clearly driven by panel buckling (where the buckling constraint boundary has been moved back to one: $KS_\mu \leq 1$). Peak thickness lobes are allocated towards the center of each panel, where the buckling eigenvector amplitude is expected to be largest. Panels with two lobes (such as at the leading edge of the root, seen in the inset of Figure 8) would indicate a bi-modal eigenvector as well. Many of the thickness design variables in this case approach the upper bound of 30 mm, which is much thicker than in the baseline of Figure 3, where the peak thickness is 23 mm. These thicker members provide a *reduction* in wing mass over the baseline, however, by providing the optimizer with greater control over the local load paths and stress concentrations, and allowing for thinner members elsewhere through the skins. The mass of this wing is 8,302.6 kg, an 8.57% reduction over the baseline. Like the baseline wing, flutter is inactive for this case. Though the buckling constraint could again be relaxed for a further mass reduction and an activation of the flutter margin to 15%, the exercise of Figure 6 is not repeated here.

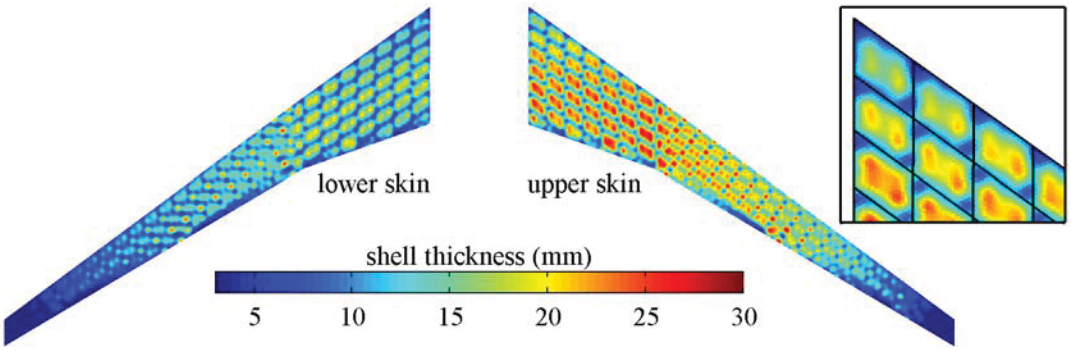

Figure 8. Optimal thickness distribution (mm) when detailed spatial variations are allowed: all rib, spar, and stringer thicknesses are at the lower bound (3 mm).

B. Functionally Graded Metals

FGM is computationally realized by assigning material fraction design variables throughout the wing, which vary between 0 (100% material A) and 1 (100% material B). The linear rule of mixtures is then used to compute the elastic modulus, yield stress, and density of the graded metal. Two scenarios are considered for FGM. The first forces the optimizer to make a choice between two metals, one of which is both heavier and stiffer than the other (aluminum and titanium, for example). Potentially, the local increase in mass would stiffen the wing (or alter the aeroelastic bend-twist coupling), allowing for a greater reduction in mass elsewhere. For the optimization statement in Eq. 6, however, the optimizer always favors the lighter of the two materials throughout the entire wing. The desire to minimize mass overrides any stiffness benefits, at least for the aeroelastic physics considered here. This overall result may also be strongly dependent on the two materials chosen.

The second scenario, which is moderately more successful, uses two metals with identical density, but one is stiffer than the other. This can be accomplished with aluminum (Al) and aluminum with silicon carbide particles (AlSiC), a metal matrix composite. It is to be expected that the optimizer will favor the stiffer AlSiC (since there is no weight penalty) for the majority of the wing, but this design will not provide a fair comparison with the baseline, which is made entirely of aluminum. To facilitate the comparison but still explore the general idea, a fictional material is paired with aluminum, which has the same density, but a 35% lower modulus and yield stress. The optimal material distribution is given in Figure 9, where a material fraction of 1 is 100% aluminum, and 0 corresponds to 100% of the weaker metal. As in Figure 8, both material and thickness design variables are assigned at the finite element level, rather than the patch level. The optimal thickness distribution looks qualitatively similar to Figure 8, and is not shown.

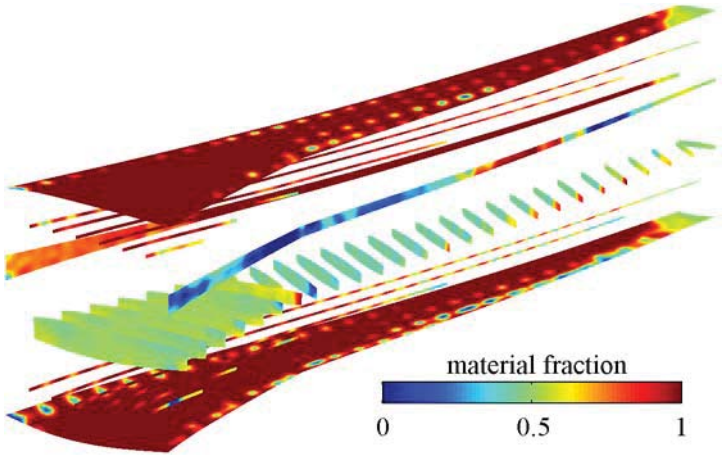

Figure 9. Material fraction distribution: a value of 1 is 100% aluminum; a value of 0 is 100% of a weaker material with the same density.

As expected, the majority of the wing (and almost all of the skins, which bear most of the load) is composed of the stiffer aluminum. Pockets of the weaker material are seen through the skins, whose localized nature would again indicate a buckling-driven phenomenon. The weaker material is also favored in the rear spar, and portions of the ribs. The rear spar design is presumably driven by a desire to increase the negative bend-twist aeroelastic coupling (wash-out), decreasing the overall wing loading [26]. The reasons for the weaker rib material are unclear, as the ribs (except near the engine attachment) bear little load. Regardless, the decrease in mass compared to the all-aluminum Figure 8 is very low: a 0.14% decrease. As above, the flutter constraint is inactive for this case.

VI. Composites

This section uses composite laminates for the upper and lower wing skins; the ribs, spars, and stringers are still composed of aluminum. Composite aircraft structural design is well within the state-of-the-art, but a conventionally-laminated design still must be considered here, in order to provide a fair comparison with tow steered designs. Composite ply material properties are listed in Table 1. In this work, ply angles are restricted to 0°, 45°, -45°, and 90° (where the 0° direction is aligned with the wing's leading edge), a typical restriction for aircraft structures rooted in certification concerns [7].

Table 1. Composite ply properties.

Parameter	Value	Parameter	Value
E_1	128 GPa	X_{1t}	1314 MPa
E_2	11 GPa	X_{1c}	1220 MPa
G_{12}	4.5 GPa	X_{2t}	43 MPa
ν_{12}	0.28	X_{2c}	168 MPa
ρ	1520 kg/m^3	S_{12}	48 MPa
t_{ply}	0.125 mm		

Ideally, optimization of composite structures would involve identifying the best laminate stacking sequence for each design patch, though this type of large-scale discrete problem is not amenable to gradient-based optimization. Alternatively, the method proposed by Liu and Haftka [27] is used here, which combines ply thickness variables and lamination parameter variables. This method recognizes the fundamental separation in roles between the in-plane membrane deformation of a composite skin laminate (dictated by the $\boldsymbol{A}$ constitutive matrix) and the out-of-plane bending deformation ($\boldsymbol{D}$ matrix). These constitutive matrices can be written as:

$$\boldsymbol{A} = (\boldsymbol{\Gamma}_0 + V_1 \cdot \boldsymbol{\Gamma}_1 + V_2 \cdot \boldsymbol{\Gamma}_2 + V_3 \cdot \boldsymbol{\Gamma}_3 + V_4 \cdot \boldsymbol{\Gamma}_4) \cdot h \tag{7}$$

$$\boldsymbol{D} = (\boldsymbol{\Gamma}_0 + W_1 \cdot \boldsymbol{\Gamma}_1 + W_2 \cdot \boldsymbol{\Gamma}_2 + W_3 \cdot \boldsymbol{\Gamma}_3 + W_4 \cdot \boldsymbol{\Gamma}_4) \cdot h^3/12 \tag{8}$$

where h is the total laminate thickness, V_i and W_i are lamination parameters, and $\boldsymbol{\Gamma}_i$ are material invariants [19].

Because the skin thickness is much less than the thickness of the airfoil, global wing deformation properties (deflection, stresses, vibration, flutter) are dominated by membrane deformation in the skins. The $\boldsymbol{A}$ matrix is independent of the stacking sequence, only depending on the *number* of plies at each orientation angle. Panel buckling deformation does depend on the $\boldsymbol{D}$ matrix, however, (due to the local bending) and so a stacking sequence choice must be made to solve the local problem. Alternatively, variations in the lamination parameters can be substituted as a pseudo-continuous way of changing the stacking sequence (permutations) for defining the $\boldsymbol{D}$ matrix. Likewise, the number of plies at each orientation (which define $\boldsymbol{A}$) can be relaxed from integer values to continuous values. In this way, gradient-based optimization can be utilized for both types of composite laminate design variables.

A. Balanced Laminates

In addition to restricting ply angles to 0°, 45°, -45°, and 90°, this section only considers balanced symmetric laminates (specially orthotropic) as well. The balance restriction is a historically typical guideline for aircraft laminates [7] in an effort to avoid undue bending/extension/torsional couplings, though arguably limits the full design capabilities of composite structures. A relaxation of the balance restriction will be considered below.

For a balanced laminate, a 45° ply must always be accompanied by a -45° ply, and so a logical design parameterization is the number of two-ply stacks for each choice: $n_{2\times0}$, $n_{\pm45}$, and $n_{2\times90}$. The laminate is then a permutation of the form $\left[(0°)_{2\cdot n_{2\times0}} / (\pm45°)_{n_{\pm45}} / (90°)_{2\cdot n_{2\times90}}\right]_s$, and the constitutive matrices are written as:

$$\boldsymbol{A} = ((n_{2\times0} + n_{\pm45} + n_{2\times90}) \cdot \boldsymbol{\Gamma}_0 + (n_{2\times0} - n_{2\times90}) \cdot \boldsymbol{\Gamma}_1 + (n_{2\times0} - n_{\pm45} + n_{2\times90}) \cdot \boldsymbol{\Gamma}_3) \cdot 4 \cdot t_{ply} \tag{9}$$

$$\boldsymbol{D} = (\boldsymbol{\Gamma}_0 + W_1 \cdot \boldsymbol{\Gamma}_1 + W_3 \cdot \boldsymbol{\Gamma}_3) \cdot \left((n_{2\times0} + n_{\pm45} + n_{2\times90}) \cdot 4 \cdot t_{ply}\right)^3 / 12 \tag{10}$$

The laminate parameters V_2, V_4, and W_4 are exactly zero for a specially orthotropic laminate, and W_2 is small enough to ignore (an approximation that becomes more accurate for thicker laminates). The laminate stiffness is then a function of 5 design variables: $n_{2\times0}$, $n_{\pm45}$, $n_{2\times90}$, W_1, and W_3. The two laminate parameters may not be chosen entirely independently of the two-ply stack variables, since not all combinations will correspond to an actual laminate. Six constraints, written in terms of the 5 design variables in Ref. [27], must be enforced to ensure feasibility.

The minimum-mass optimization process is similar to that used for the baseline, where composite design variables include $n_{2\times0}$, $n_{\pm45}$, $n_{2\times90}$, W_1, and W_3 for each of the upper and lower skin panels in Figure 2, and metallic thickness patch design variables in the ribs, spars, and stringers. KS_f and KS_μ constraints are spread across the same three static load cases (though KS_f metrics must now consider Tsai-Wu failure metrics in all four ply orientations for composite panels), and the flutter constraint KS_{fl} is enforced as above. Six laminate feasibility constraints are included per panel as well. Explicit manufacturing constraints that dictate ply addition and deletion between adjacent panels are not included here, but all design variables are again passed through a spatial filter that will prevent large lay-up differences between adjacent panels.

The resulting optimal distribution of two-ply stacks through the skins is seen in Figure 10; all metallic thickness variables in the ribs, spars, and stringers have gone to the lower bound of 3 mm, as above. The mass of this composite wing is 5,669.2 kg, a 37.57% drop from the baseline. Similar mass improvements between metallic and composite wings via aeroelastic optimization have been noted in Ref. [18]. The flutter constraint is active for this wing, but not strongly so: removing the constraint results in less than a 0.01% reduction in optimal wing mass. The flutter mechanism is very similar to that seen in Figure 7, and is not shown.

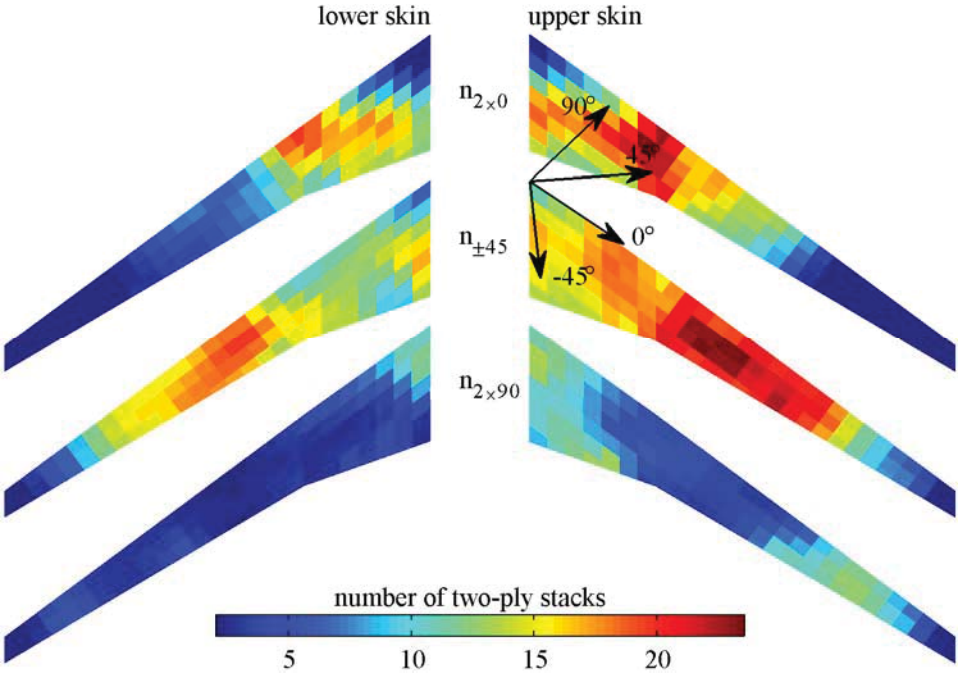

Figure 10. Optimal distribution of two-ply stacks throughout the wing skins.

The composite thickness distributions mirror the overall trend of the baseline's metallic thicknesses. 0° plies are most-prominently used at the wing break, where the bending stresses are known to be largest. Stacks of ±45° fibers are allocated farther outboard, where torsional stresses of the rolling maneuver are highest (as seen in Figure 4) from the third maneuver load case, and some 90° plies are used at the wing root and tip. The peak thickness of this wing is 23.2 mm (computed by $(n_{2\times0} + n_{\pm45} + n_{2\times90}) \cdot 4 \cdot t_{ply}$, where the factor of 4 reflects both the balance and the symmetry requirements), which is comparable to that found for the metallic baseline. W_1 and W_3 lamination parameters are shown throughout the wing in Figure 11. As noted, these design variables are primarily used by the optimizer to satisfy the local panel buckling constraints and must be chosen to satisfy laminate feasibility constraints as well, which are active throughout the wing. An inverse process could be conducted to convert each W_1 - W_3 pair into an actual laminate stacking sequence, but this is not done here. Contiguous ply constraints (where no more than 4 plies of the same orientation can lie next to each other in the stacking sequence, owing to matrix cracking issues) cannot be included in the laminate parameterization framework used here [27].

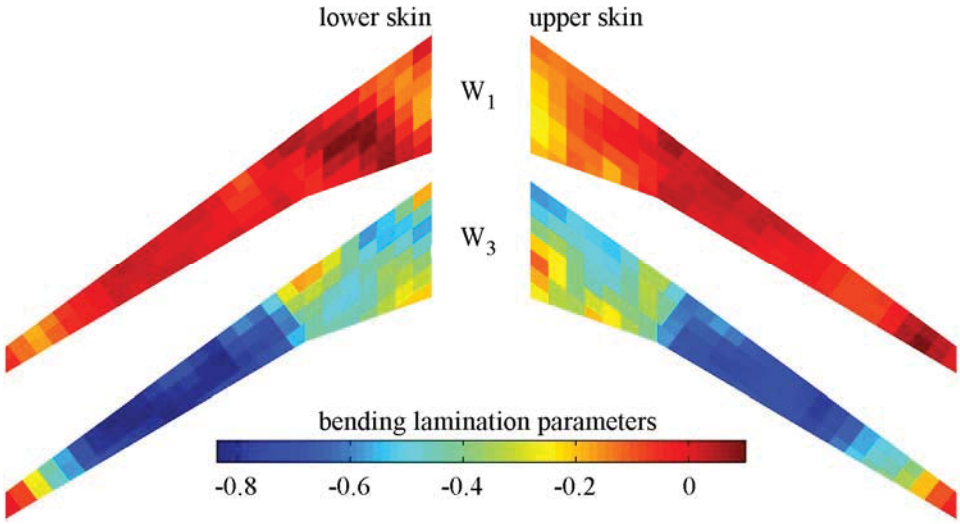

Figure 11. Lamination parameters corresponding to the balanced composite structure in Figure 10.

B. Balanced Tow Steered Laminates

In this work, separate laminate steering paths are identified for each rib bay, as shown in Figure 12. A local coordinate system is set up for each bay, whose origin lies at the bay center, with an x-axis parallel to the straight 0° fibers (parallel to the wing leading edge). Similar to the approach in Ref. [28], the steering angle ϕ is defined as a piecewise-linear curve within the rib bay. Three control points are used here, whose magnitudes are design variables controlled by the optimizer. This results in a curvilinear steering path seen on the right of Figure 12. Along the rib bay's x-axis, the fiber angles vary according to the prescribed curve, whereas perpendicular to the axis, the steering angles are constant. Steering continuity is enforced across adjacent rib bays, in the sense that ϕ_3 will be identical, in both location and magnitude, to ϕ_1 of the next outboard rib bay. This continuity allows the entire wing skin to be built as a monolithic structure.

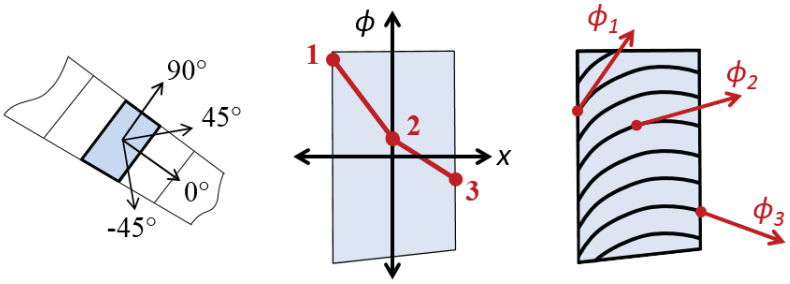

Figure 12. Fiber angles dictated by piecewise-linear splines (three control points per rib bay), resulting in curvilinear tow paths.

In theory, each ply in a laminate can be steered independently, though the resulting laminate would not, in general, be composed of only 0°, 45°, -45°, and 90° fibers. This feature (special orthotropy) is to be preserved in order to continue the use of the parameterization scheme implemented above. A second reason is that, at present, laminate fiber angles are typically restricted to a finite set for certification reasons. Specially orthotropic laminates can be utilized in a steering environment by laying all of the 0° stacks in a laminate along the actual steering path shown in Figure 12. All 90° stacks are placed along courses perpendicular to this path, and ±45° layers are similarly steered, seen in Figure 13. Globally, fiber angles can take any value, but locally, each point in each panel has the same laminate (same number of two-ply stacks, same stacking sequence) [5].

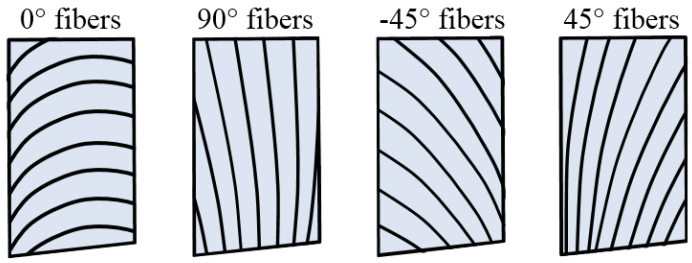

Figure 13. Steering paths of the 0°, 45°, -45°, and 90° degree fibers, for the example in Figure 12.

The aeroelastic optimization process proceeds in a similar way as in the previous exercise. The number of design variables per panel is the same ($n_{2\times0}$, $n_{\pm45}$, $n_{2\times90}$, W_1, and W_3), but the design variable vector is now augmented by tow steering control knots at rib locations and rib bay center locations. Separate steering paths are designed for the upper and the lower wing skins. The resulting optimal steering patterns in the wing are shown in Figure 14. The remaining design variables are qualitatively similar in overall distribution to the previous result and will not be shown, but the mass of this tow steered structure is 5,328.4 kg. This is a 41.32% improvement over the metallic baseline, and perhaps more relevant, a 6.01% improvement over the conventional laminate result of Figure 10. As with the un-steered result, the flutter constraint is active for this steered design.

The most prominent use of steering path curvature seen in Figure 14 is around the trailing edge wing break of the lower skin, where the parameterization has smoothed the structure around the discontinuity in the wing geometry. This reduces the known stress concentration in the region and allows the optimizer to remove material here. Local undulations in the steering curvature are notable along the inboard portions of the upper skin and are presumably driven by the panel buckling constraints. Similar steering patterns are utilized in Ref. [29] for panel buckling.

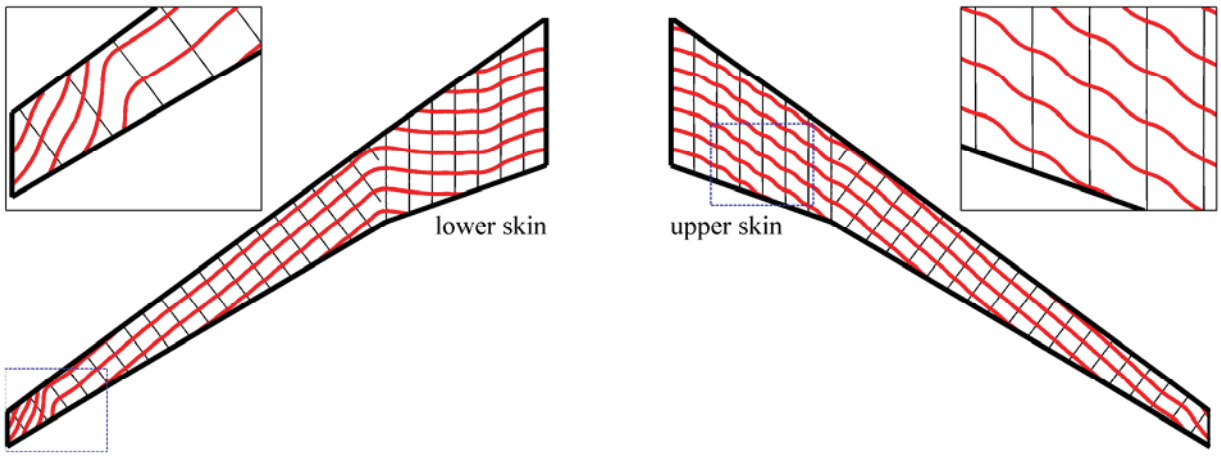

Figure 14. Steering patterns (fiber directions of the 0° stacks) over the optimal tow steered composite wing constructed of balanced laminates.

Some rib bays, including many outboard of the wing break on both the upper and lower skins, do not exhibit much curvature. It is unclear whether the dominating physical phenomena in these bays (such as the buckling

modes) actually prefer straight fibers, or whether this result is a local-minima. Some of these straight-fibered areas have exploited the tow steering parameterization used here to rotate their entire laminate relative to the leading edge, by using near-equal values for all three control points in Figure 12. The fibers are straight, but the 0° stacks are no longer parallel to the leading edge of the wing. As such, the comparison between the tow steered and straight fiber results (6.01% reduction in mass) may not be a fair referendum on the advantages of curvilinear tow paths.

C. Unbalanced Laminates

This section removes the balance restriction imposed above. Ply angles are still limited to 0°, 45°, -45°, and 90°, but the number of 45° plies can now be different from the number of -45° plies. Unbalanced laminates can be tailored to have large bending/torsion coupling (the D_{16} and D_{26} terms), whereas these coupling terms are relatively small for balanced laminates, and tend to zero as the number of plies increases [27]. Given that the bending/torsion coupling of unbalanced laminates has historically been a key driver for aeroelastic tailoring [26], a certain performance improvement is expected over balanced laminates in the current setting.

The design parameterization used here is the number of single-ply stacks for each ply angle: n_0, n_{45}, n_{-45}, and n_{90}. The laminate is then a permutation of the form $\left[(0°)_{n_0} / (45°)_{n_{45}} / (-45°)_{n_{-45}} / (90°)_{n_{90}}\right]_s$, and the constitutive matrices are written as:

$$\boldsymbol{A} = \begin{pmatrix}(n_0 + n_{45} + n_{-45} + n_{90}) \cdot \boldsymbol{\Gamma}_0 + (n_0 - n_{90}) \cdot \boldsymbol{\Gamma}_1 + \\ (n_{45} - n_{-45}) \cdot \boldsymbol{\Gamma}_2 + (n_0 - n_{45} - n_{-45} + n_{90}) \cdot \boldsymbol{\Gamma}_3\end{pmatrix} \cdot 2 \cdot t_{ply} \tag{11}$$

$$\boldsymbol{D} = (\boldsymbol{\Gamma}_0 + W_1 \cdot \boldsymbol{\Gamma}_1 + W_2 \cdot \boldsymbol{\Gamma}_2 + W_3 \cdot \boldsymbol{\Gamma}_3) \cdot \left((n_0 + n_{45} + n_{-45} + n_{90}) \cdot 2 \cdot t_{ply}\right)^3 / 12 \tag{12}$$

The laminate parameters V_4 and W_4 are zero for this case. Each unbalanced laminate is then defined by seven design variables: n_0, n_{45}, n_{-45}, n_{90}, W_1, W_2, and W_3. As above, the three laminate parameters may not be chosen independently of the single-ply stack variables: feasibility constraints must be met. For an unbalanced laminate restricted to 0°, 45°, -45°, and 90° ply angles, there are 26 total feasibility constraints, listed in Ref. [30]. This section considers only straight fibers (no tow steering) and design optimization proceeds as in Section VI-A, albeit with more design variables (7, as opposed to 5) and more laminate feasibility constraints (26, as opposed to only 6 previously) per composite panel.

The optimal result is seen in Figure 15 and Figure 16, for the distribution of one-ply stacks and the lamination parameters, respectively. The mass of this wing structure is 5,410.0 kg, the flutter constraint is again active, and the peak thickness is 23.1 mm (computed by $(n_0 + n_{45} + n_{-45} + n_{90}) \cdot 2 \cdot t_{ply}$, where the factor of 2 reflects the symmetry requirement), which is comparable to both the metallic baseline and the balanced laminate design. The mass reduction is a 40.42% improvement over the metallic baseline, but the more-relevant comparison for this unbalanced laminate structure is with the balanced laminate structure of Figure 10, and a 4.56% improvement is seen here. This is less of an improvement than may be expected given the important role that unbalanced laminates play in dictating bend-twist coupling and static aeroelastic physics [26].

It may be that the ability to separately tailor the upper and lower skins (which is an available design feature for all parameterizations considered here) provides enough control over global wing-level bend twist coupling, and localized unbalanced laminates cannot add much improvement beyond this. Furthermore, it may be found that this design, like all the others in this paper, is a local minimum, though additional starting points for the optimization were not found to obtain appreciably different optima than those shown in Figure 15 and Figure 16. Regardless, unbalanced laminates are exploited by the optimizer throughout the wing, as evidenced by large spatial distribution differences between n_{45} and n_{-45}, and by large values of W_2, neither of which is a design option available to the balanced case. Substantial differences in the allocation of 0° plies are further noted for this unbalanced case (as opposed to the balanced case of Figure 10) as well, where more of this material is allocated at the wing root than the wing break.

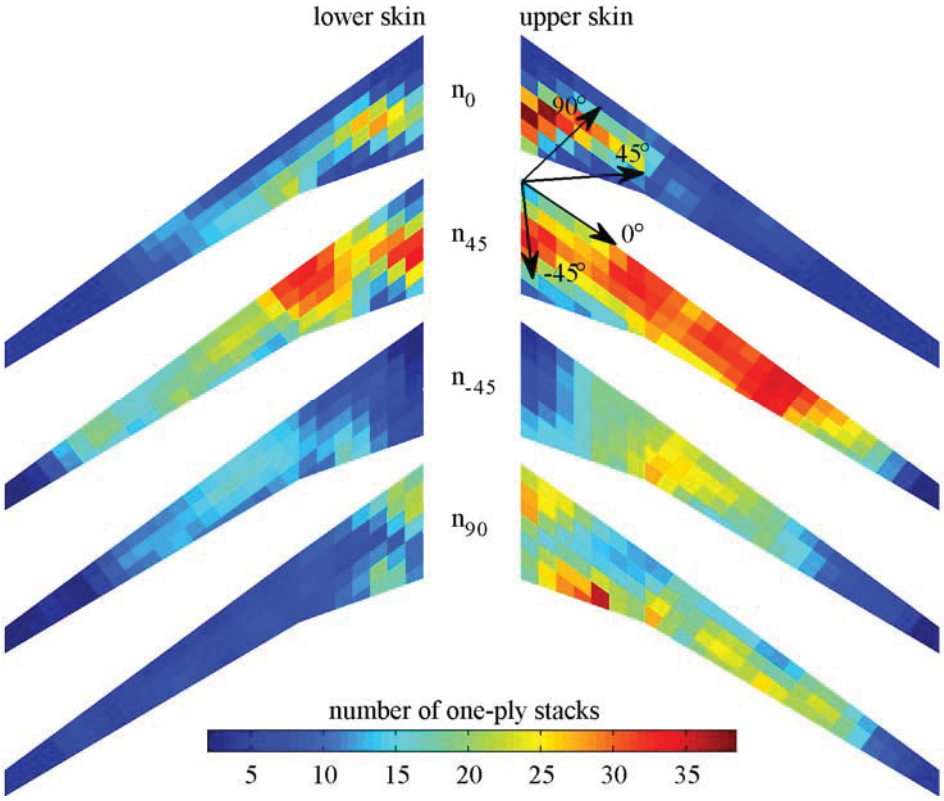

Figure 15. Optimal distribution of one-ply stacks throughout the wing skins.

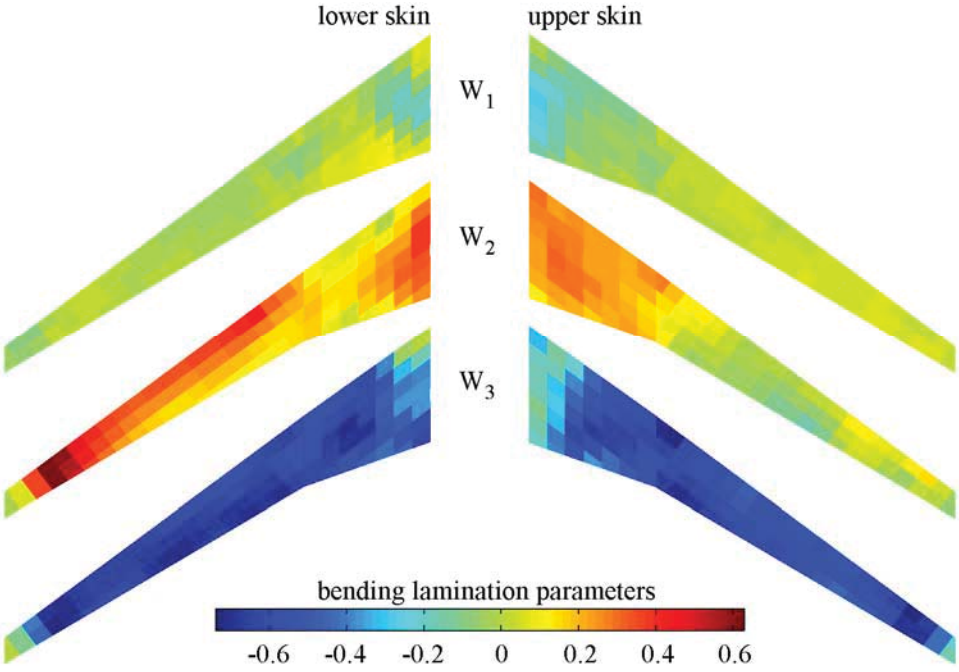

Figure 16. Lamination parameters corresponding to the unbalanced composite structure in Figure 15.

D. Unbalanced Tow Steered Laminates

The final composite design parameterization used here combines the unbalanced laminates of Section VI-C with the tow steering concepts of Section VI-B. The design variables for each panel are n_0, n_{45}, n_{-45}, n_{90}, W_1, W_2, and W_3, and tow steering control knots at rib locations and rib bay center locations are designed as well. The optimal distribution of laminate stiffness is qualitatively similar to Figure 15 and Figure 16, and is not shown here. The optimal steering patterns for this case are shown in Figure 17. The flutter constraint for this structure is active, and its mass is 5,323.9 kg. This is a 41.38% drop over the metallic baseline, a 1.61% drop relative to the un-steered unbalanced case, and a 0.09% drop relative to the steered balanced case. The optimal steering pattern for this case is qualitatively similar to that seen for the balanced case (Figure 14), though the curvature about the wing break of the lower skins is far less pronounced. This is presumably due to the fact that the design parameterization for unbalanced panels already provides the optimizer with enough control over the large stress concentration in this region, without a strong need for additional steering.

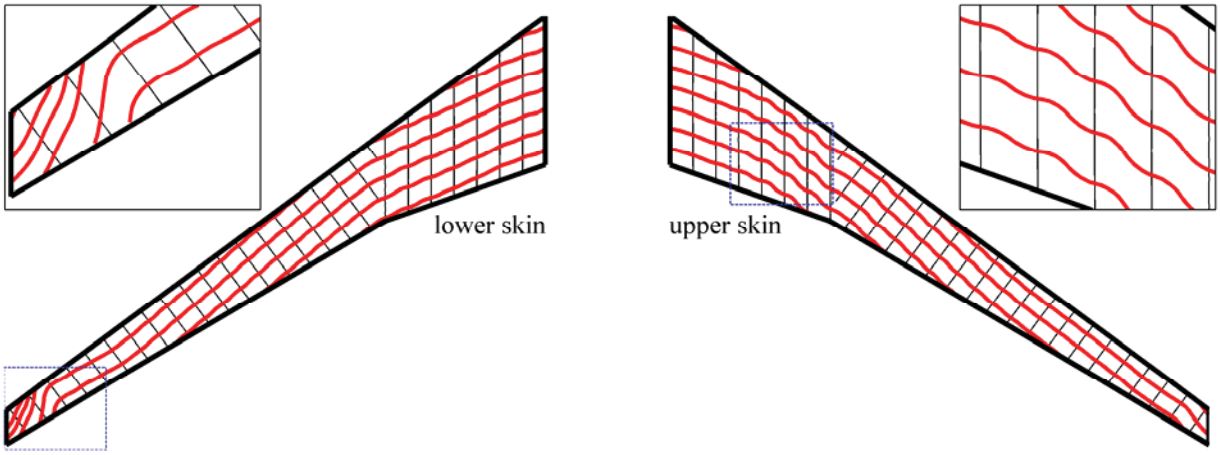

Figure 17. Steering patterns (fiber directions of the 0° stacks) over the optimal tow steered composite wing constructed of unbalanced laminates.

VII. Distributed Control Surfaces

The final aeroelastic tailoring scheme returns to the all-metallic patch-based thickness-design-variable methods used for the baseline (Figure 3), but also includes the scheduling of distributed control surfaces along the trailing edge ($\boldsymbol{\gamma}$ in Eqs. 1 and 2) as design variables as well. Simultaneous handling of wing structure design variables and control surface scheduling design variables, within the same optimization loop, is in contrast to most of the existing literature on this topic (see Ref. [31] and papers cited within). Control surface deflections and other trim variables are typically computed within an inner loop (via an over-determined trim optimization process), and structural design variables are optimized through an outer loop. This is due to the limitations of certain codes that can conduct structural optimization but not trim optimization. In this work, the use of the adjoint method for aeroelastic gradients enables simultaneous optimization of both sets of design variables, which is presumably more efficient. It should be recalled that, whatever control surface deflections $\boldsymbol{\gamma}$ are imposed by the optimizer, the aeroelastic analysis (Eqs. 1 and 2) will automatically locate the variables that trim the aircraft (α and δ for longitudinal maneuvers, and α and β for lateral).

The trailing edge of the wing is discretized into 20 control surfaces from root to tip, each with a hinge line at 71% of the local chord. This results in 80 total control surface design variables: one set each for the longitudinal load cases 1 and 2 (pull-up and push-over maneuvers), and two sets for the rolling load case 3 (a symmetric and an anti-symmetric scheduling). As above, the separation between symmetric and anti-symmetric physics is possible due to the linearity of the system, and total control surface deflections are eventually found by summing $\boldsymbol{\gamma}^s$ and $\boldsymbol{\gamma}^a$ (or subtracting them, for the left wing). Hinge moment constraints are imposed for each control surface, as well as side limits of ±20°. As with structural design variables, the scheduling variables, for a given load case, are passed through a spatial filter in order to maintain a smooth deflection along the trailing edge.

The optimal control surface scheduling is shown in Figure 18 and Figure 19. Positive flap deflection corresponds to a tip-down rotation of the surface, as is conventional [16]. For maneuver load 1 (2.5g pull-up),

additional lift is generated in-board, to maintain the overall lift-based trim of the aircraft, but load alleviation is used out-board, in order to reduce the total bending moment on the wing. This allows the optimizer to remove material from the structure (reducing mass, the ultimate objective function) without violating the strength and buckling constraints. Tip-up rotations of all of the control surfaces, from root to tip, would *explicitly* reduce the stresses and buckling loads even more, but the *implicit* effect would be an ultimate increase in α to maintain trim, and thus an increase in the aerodynamic loading.

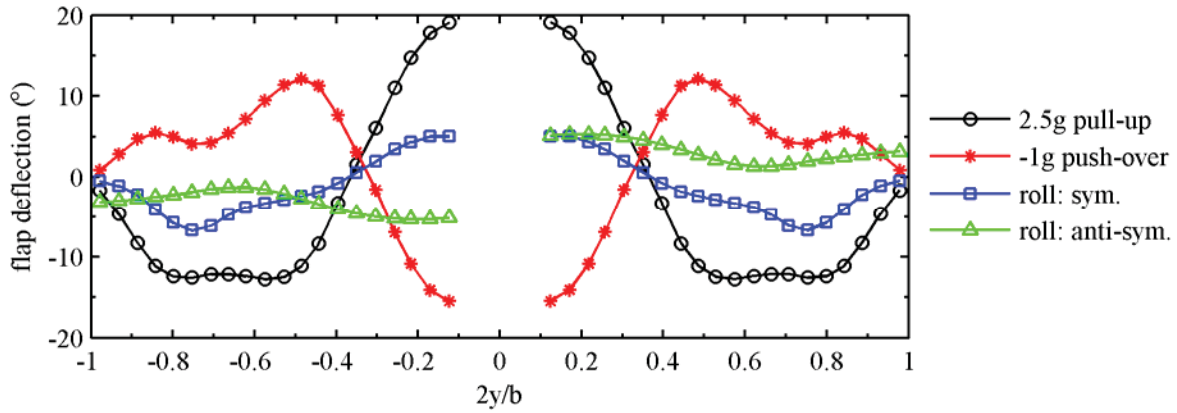

Figure 18. Optimal control surface scheduling for each load case.

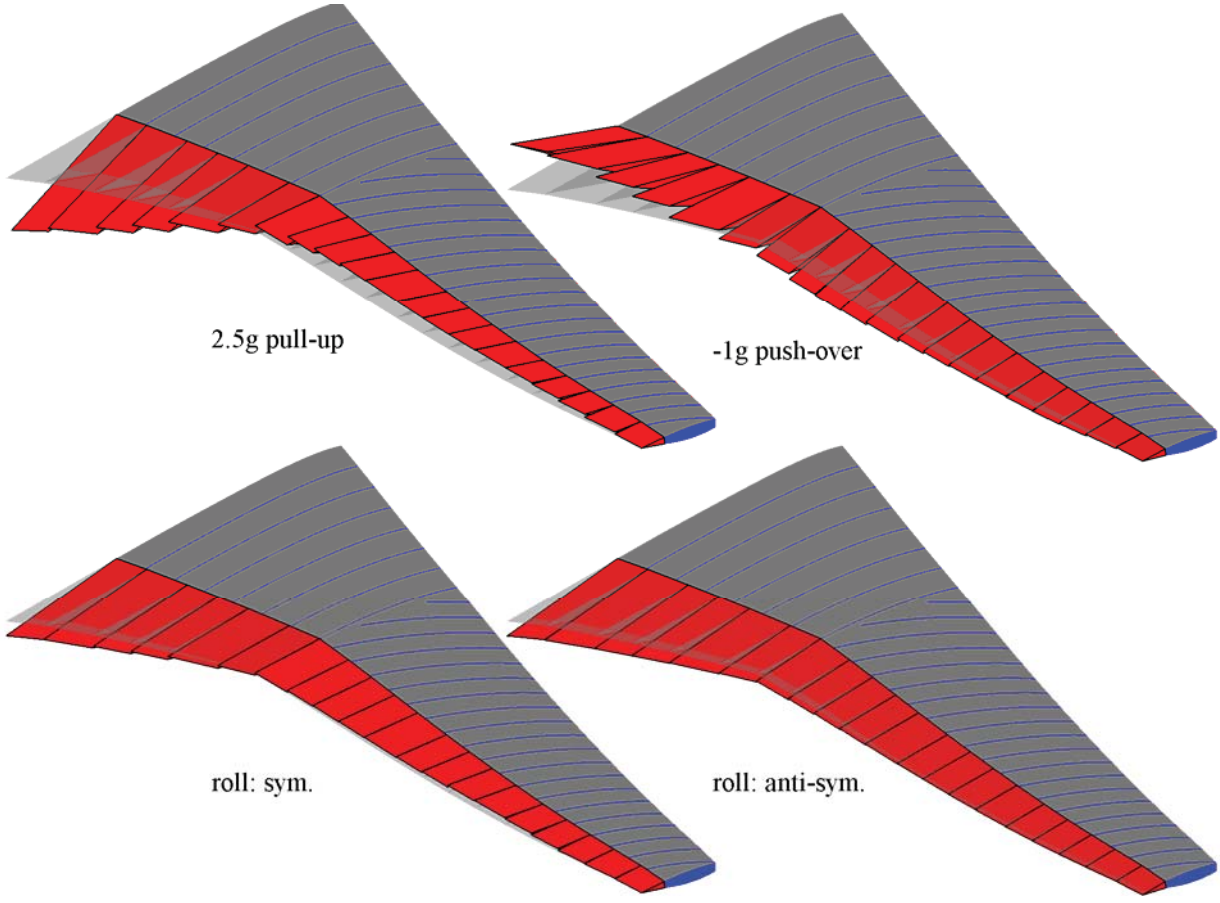

Figure 19. Qualitative picture of control surface schedules corresponding to data in Figure 18.

Control surface scheduling for load case 2 (-1g push-over) has the expected opposite trends (but lower magnitude) as compared to the 2.5g pull-up maneuver. For load case 3, the symmetric deflections are responsible (along with the angle of attack α) for maintaining steady level flight (N=1). As such, the symmetric scheduling has the same trends as load case 1, though the amplitudes are obviously smaller. The anti-symmetric deflections are responsible for maintaining a steady roll rate ($p \cdot L/U$ = 0.065, as in all the cases in this paper), and so this is accomplished with a moderate tip-down rotation of all the control surfaces, with peak amplitude at the wing root. In-board surface rotations are obviously less effective than outboard at generating a rolling moment, but they impose less torsional stress as well, and so the anti-symmetric scheduling shown in Figure 18 and Figure 19 is the optimal compromise.

The optimal patch-based metallic thickness variables are shown in Figure 20: the optimal mass of this structure is 4,978.5 kg, a substantial 45.18% reduction over the baseline. Overall skin thicknesses have dropped considerably compared to this baseline, with many lower skin panels approaching the 3 mm lower bound. Peak thickness in the upper skin has been pushed from the wing break (as seen in Figure 3) to the leading edge root. Shell thicknesses in the ribs and spars, as with the other results in this paper, all reside at the lower bound of 3 mm. Though not explicitly shown here, the structural deformation of this wing is dominated by torsional deflection (for all three static load cases), whereas the other optimal structures display a bending-dominant response. Furthermore, the flutter constraint is strongly active for this lightweight structure, which will be explored in more detail below.

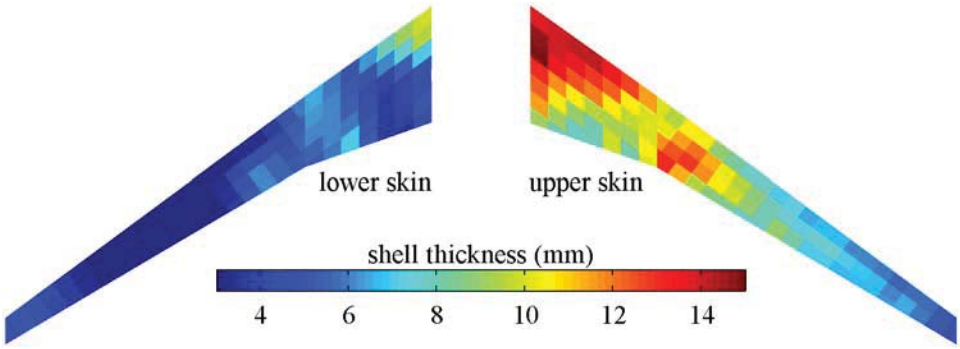

Figure 20. Optimal thickness distribution (mm) for the case where structural thicknesses and control surface scheduling are designed simultaneously.

Perhaps more than any other result in this paper, the optimal structure in Figure 20 should be qualified in terms of modeling omissions, which will surely force an increase in minimum mass. An explicit structural model of each control surface and its mechanism is ignored here, as are the attachment details of each mechanism to the spars. The lumped mass distribution through the trailing edge (seen in Figure 1) is not updated when more control surfaces are included (yet this inclusion may cancel out as each mechanism will be smaller as well). Furthermore, the detrimental maneuver drag load induced by these control surfaces has not been factored into the optimization process. Nonetheless, the exercise in this section has demonstrated the ability to simultaneously optimize both wing structure and control surface scheduling, where the optimizer is able to exploit the conflict between aeroelastic trim and strength/buckling towards a minimum-mass structure.

A. Flutter-Mass Pareto Front

As noted, the flutter constraint is strongly active for the low-mass wing structure in Figure 20, and it is of interest to ascertain how much additional mass could be removed by relaxing this constraint. Unlike the buckling constraint, where linear failure boundaries may be non-conservative and thus warrant possible relaxation (as seen in Figure 6), the flutter constraint is a rapid and catastrophic failure mode well-predicted by linearized physics. Nonetheless, it may be possible to relax the open-loop flutter margin for additional weight reduction, with the future goal of re-obtaining the required 15% margin with close-loop control. For the current case, the prescribed static deflection of the trailing edge control surfaces could be used to alleviate maneuver loads (as demonstrated here), on top of which a small oscillatory deflection is superimposed [32], to obtain the required closed-loop flutter margin.

Aeroservoelastic effects are beyond the scope of the current work, but the Pareto front between optimal weight and allowable open-loop flutter margin is shown in Figure 21. The design variables for this exercise are the same as in Figure 19 and Figure 20. The flutter constraint becomes inactive below an allowable flutter margin of -20%: removing the flutter constraint entirely provides an optimum wing mass of 4,810.3 kg. Comparing this to the design

that meets the 15% flutter margin (shown in Figure 19 and Figure 20), a maximum mass reduction of 3.37% is available. If the open-loop margin is only relaxed to 10% (a more realistic situation), the mass reduction drops to 0.52%. Furthermore, these mass reduction values must also be offset by the instrumentation required for the feedback control of a distributed bank of oscillating trailing edge control surfaces.

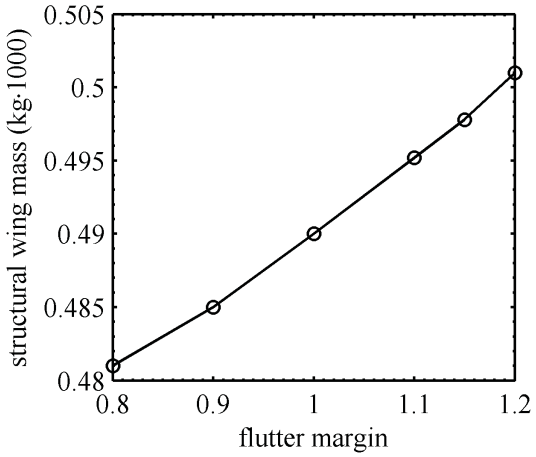

Figure 21. Pareto front between allowable flutter margin and optimal wing mass.

VIII. Conclusions

An overall summary of the six optimal wing structures presented in this paper is provided in Table 2. All are subject to the same 3 trimmed static aeroelastic load cases, under the same set of strength and panel buckling constraints, as well as a transonic flutter constraint (which is only active for the lighter-weight wing designs 4-8). These minimum-mass optimization studies are entirely enabled by the computation of analytical adjoint-based aeroelastic gradients, which facilitate problems with a large number of structural, material, and flap scheduling design variables (ranging in number from 10^2 to 10^5) under a large number of constraints (between 10^2 and 10^3). Transonic flutter boundaries are approximated with the ZTRAN tool.

The most relevant comparison point, in terms of mass-reduction, is listed in the table for each design. The lowest wing mass, as compared to the baseline, can be obtained with distributed trailing edge control effectors (45.18%), though the many caveats associated with this design have been discussed above. A switch in wing skin material from aluminum to balanced composite laminates also enables a sizeable reduction in mass (37.57%). Further reductions are available with the implementation of tow steering (6.01% relative to the design with straight fibers), unbalanced laminates (4.56%), or both. Allowing for a highly detailed metallic thickness distribution through the structure provides a moderate reduction in mass (8.57%), but the improvement via FGM is very muted: 0.14%. Though not captured in Table 2, this work has also explored the effects of relaxing the buckling constraint, or the flutter constraint, by computing the complete Pareto front.

Table 2. Summary of optimal wing structures.

Design Number	Description	Structural Wing Mass (kg)	Best Design for Mass Comparison	% Mass Reduction	Figure
1	baseline: patch thickness variables	9,081.3	-	-	Figure 3
2	spatially-detailed thickness variations	8,302.6	1	8.57%	Figure 8
3	functionally graded metals	8,290.3	2	0.14%	Figure 9
4	balanced straight laminates	5,669.2	1	37.57%	Figure 10
5	balanced tow steered laminates	5,328.4	4	6.01%	Figure 14
6	unbalanced straight laminates	5,410.0	4	4.56%	Figure 15
7	unbalanced tow steered laminates	5,323.9	6	1.61%	Figure 17
8	distributed control surfaces	4,978.5	1	45.18%	Figure 20

A key question with each of these designs remains unresolved: is the reduction in wing weight (which will implicitly result in a cost reduction through reduced fuel, among other benefits) enough to offset the increased manufacturing costs? Some of the techniques in Table 2 are far enough beyond the current state-of-the-art (for large acreage structures, in any case) that this question will prove very difficult to answer. Others are perhaps more feasible, and a performance/cost trade-off may be conducted. Manufacturing costs may also be incorporated directly into the optimization process, on a member-by-member basis. For example, on purely physical grounds, both panel A and panel B may benefit from the use of an advanced tailoring scheme, but the optimizer may exploit the knowledge that the use of this tool is only warranted in panel B, as the performance improvement in panel A is not enough to offset the manufacturing cost.

Acknowledgements

This work is funded by the Fixed Wing project under NASA's Fundamental Aeronautics Program.

References

[1] Stanford, B., Jutte, C., "Trim and Structural Optimization of Subsonic Transport Wings using Nonconventional Aeroelastic Tailoring" *AIAA Aviation Conference*, Atlanta, GA, June 16-20, 2014.

[2] Birman, V., Byrd, L., "Modeling and Analysis of Functionally Graded Materials and Structures," *Applied Mechanics Reviews*, Vol. 60, No. 5, pp. 195-216, 2007.

[3] Librescu, L., Maalawi, K., "Material Grading for Improved Aeroelastic Stability in Composite Wings," *Journal of Mechanics of Materials and Structures*, Vol. 2, No. 7, pp. 1381-1394, 2007.

[4] Stodieck, O., Cooper, J., Weaver, P., Kealy, P., "Improved Aeroelastic Tailoring Using Tow-Steered Composites," *Composite Structures*, Vol. 106, pp. 703-715, 2013.

[5] Stanford, B., Jutte, C., Wu, K., " Aeroelastic Benefits of Tow Steering for Composite Plates," *Composite Structures*, Vol. 118, pp. 416-422, 2014.

[6] Urnes, J., Nguyen, N., Ippolito, C., Totah, J., Trinh, K., Ting, E., "A Mission-Adaptive Variable Camber Flap Control System to Optimization High Lift and Cruise Lift-to-Drag Ratios of Future N+3 Transport Aircraft," *AIAA Aerospace Sciences Meeting*, Grapevine, TX, January 7-10, 2013.

[7] Niu, M., *Airframe Structural Design*, Conmilit Press Ltd., Hong Kong, 1988.

[8] Yurkovich, R., "Status of Unsteady Aerodynamic Prediction for Flutter of High-Performance Aircraft," *Journal of Aircraft*, Vol. 40, No. 5, pp. 832-842, 2003.

[9] Zhang, Z., Yang, S., Chen, P., "Linearized Euler Solver for Rapid Frequency-Domain Aeroelastic Analysis," *Journal of Aircraft*, Vol. 49, No. 3, pp. 922-932, 2012.

[10] Stanford, B., Beran, P., "Direct Flutter and Limit Cycle Computations of Highly Flexible Wings for Efficient Analysis and Optimization," *Journal of Fluids and Structures*, Vol. 36, pp. 111-123, 2013.

[11] Chen, P., Gao, X., Tang, L., "Overset Field-Panel Method for Unsteady Transonic Aerodynamic Influence Coefficient Matrix Generation," *AIAA Journal*, Vol. 42, No. 9, pp. 1775-1787, 2004.

[12] Vassberg, J., DeHaan, M., Rivers, S., Wahls, R., "Development of a Common Research Model for Applied CFD Validation Studies," AIAA Applied Aerodynamics Conference, Honolulu, Hawaii, August 10-13, 2008.

[13] Cook, R., Malkus, D., Plesha, M., Witt, R., *Concepts and Applications of Finite Element Analysis*, Wiley, New York, 2002.

[14] Katz, J., Plotkin, A., *Low-Sped Aerodynamics*, *Cambridge University Press*, Cambridge, UK, 2001.

[15] Appa, K., "Finite-Surface Spline," *Journal of Aircraft*, Vol. 26, No. 5, pp. 495-496, 1989.

[16] Bisplinghoff, R., Ashley, H., Halfman, R., *Aeroelasticity*, Addison-Wesley, Cambridge, MA, 1955.

[17] Kreisselmeier, G., Steinhauser, R., "Systematic Control Design by Optimizing a Vector Performance Index", *International Federation of Active Controls Symposium on Computer-Aided Design of Control Systems*, Zurich, Switzerland, 1979.

[18] Kennedy, G., Martins, J., "A Comparison of Metallic and Composite Aircraft Wings using Aerostructural Design Optimization," *AIAA Aviation Technology, Integration, and Operations Conference*, Indianapolis, IN, September 17-19, 2012.

[19] Dillinger, J., Klimmek, T., Abdalla, M., Gürdal, Z., "Stiffness Optimization of Composite Wings with Aeroelastic Constraints," *Journal of Aircraft*, Vol. 50, No. 4, pp. 1159-1168, 2013.

[20] Hassig, H., "An Approximate True Damping Solution of the Flutter Equation by Determinant Iteration," *Journal Of Aircraft*, Vol. 8, No. 11, pp. 885-889, 1971.

[21] van Zyl, L., Maserumule, M., "Divergence and the p-k Flutter Equation," *Journal of Aircraft*, Vol. 38, No. 3, pp. 584-586, 2001.

[22] Ringertz, U., "On Structural Optimization with Aeroelasticity Constraints," *Structural Optimization*, Vol. 8, pp. 16-23, 1994.

[23] Haftka, R., Gürdal, Z., *Elements of Structural Optimization*, Kluwer Academic Publishers, Dordecht, The Netherlands, 1992.

[24] Sigmund, O., "Morphology-Based Black and White Filters for Topology Optimization," *Structural and Multidisciplinary Optimization*, Vol. 33, pp. 401-424, 2007.

[25] Svanberg, K., "A Class of Globally Convergent Optimization Methods Based on Conservative Convex Separable Approximations," *SIAM Journal of Optimization*, Vol. 12, pp. 555-573, 2002.
[26] Shirk, M., Hertz, T., Weisshaar, T., "Aeroelastic Tailoring – Theory, Practice, and Promise," *Journal of Aircraft*, Vol. 23, No. 1, pp. 6-18, 1986.
[27] Liu, B., Haftka, R., "Single-Level Composite Wing Optimization Based on Flexural Lamination Parameters," *Structural and Multidisciplinary Optimization*, Vol. 26, pp. 111-120, 2004.
[28] Alhajahmad, A., Abdalla, M., Gürdal, Z., "Optimal Design of Tow-Placed Fuselage Panels for Maximum Strength with Buckling Considerations," *Journal of Aircraft*, Vol. 47, No. 3, pp. 775-782, 2010.
[29] Weaver, P., Potter, K., Hazra, K., Saverymuthapulle, M., Hawthorne, M., "Buckling of Variable Angle Tow Plates: from Concept to Experiment," *AIAA Structures, Structural Dynamics, and Materials Conference*, Palm Springs, CA, May 4-7, 2009.
[30] Diaconu, C., Sekine, H., "Layup Optimization for Buckling of Laminated Composite Shells with Restricted Layer Angles," *AIAA Journal*, Vol. 42, No. 10, pp. 2153-2163, 2004.
[31] Zink, P., Mavris, D., Raveh, D., "Maneuver Trim Optimization Techniques for Active Aeroelastic Wings," *Journal of Aircraft*, Vol. 38, No. 6, pp. 1139-1146, 2001.
[32] Livne, E., "Integrated Aeroservoelastic Optimization: Status and Direction," *Journal of Aircraft*, Vol. 36, No. 1, pp. 122-145, 1999.